

# Equiaxed Dendritic Solidification with Convection: Part III. Comparisons with $\text{NH}_4\text{Cl-H}_2\text{O}$ Experiments

C. BECKERMANN and C.Y. WANG

This third article on equiaxed dendritic solidification is intended to provide experimental validation of the multiphase model developed in part I. Numerical and experimental results are presented for the solidification of a  $\text{NH}_4\text{Cl-70 wt pct H}_2\text{O}$  solution inside a square cavity cooled equally from all sidewalls. The numerical simulations were performed using the numerical procedures developed in part II. The experiments were conducted to measure the temperature histories *via* thermocouples and to record the images of the solidification process using a shadowgraph system. Preliminary validity of the multiphase model is demonstrated by the qualitative agreement between the measurements and predictions of cooling curves as well as of the evolution of the crystal sediment bed. In addition, several important features of equiaxed dendritic solidification are identified through this combined experimental and numerical study, including the grain generation and growth behaviors in the presence of liquid flow, the sedimentation of equiaxed crystals, the formation of a crystal sediment bed, and a bottom zone of negative segregation resulting from the countercurrent solid-liquid multiphase flow. Quantitative comparisons between the numerical simulation and experiment reveal several areas for future research.

## I. INTRODUCTION

SIMULTANEOUS liquid and solid flow is an important, but little understood, phenomenon in equiaxed alloy solidification. Convection in the liquid melt is caused by both thermal and solutal buoyancy forces, while the movement of free solid crystals is due to the density difference between solid and liquid under the influence of gravity. The resulting solid-liquid multiphase flow pattern strongly depends on the microstructure of the equiaxed crystals which, in turn, is governed by grain nucleation and growth mechanisms. Wang *et al.*<sup>[1]</sup> have shown that the settling characteristics of equiaxed crystals in the free particle regime and the permeability of the liquid melt through a packed bed of equiaxed grains are functions not only of the solid and grain fractions but also the multiple length scales characteristic of an equiaxed dendritic morphology. Because the coupled solid-liquid flow causes structural and chemical inhomogeneities in final solidified products, a fundamental understanding of the multiphase transport phenomena coupled with the grain nucleation and growth mechanisms is required.

In a multiphase model formulated by the present authors for equiaxed dendritic solidification<sup>[2]</sup> (hereinafter referred to as part I), the multiphase transport occurring on the macroscopic (system) scale has been coupled with the grain nucleation and growth mechanisms taking place on various microscopic scales. It has been further shown in Reference 3 (hereinafter referred to as part II) that such a micro-macroscopic modeling approach is capable of predicting grain structure and macrosegregation. The objective of the pres-

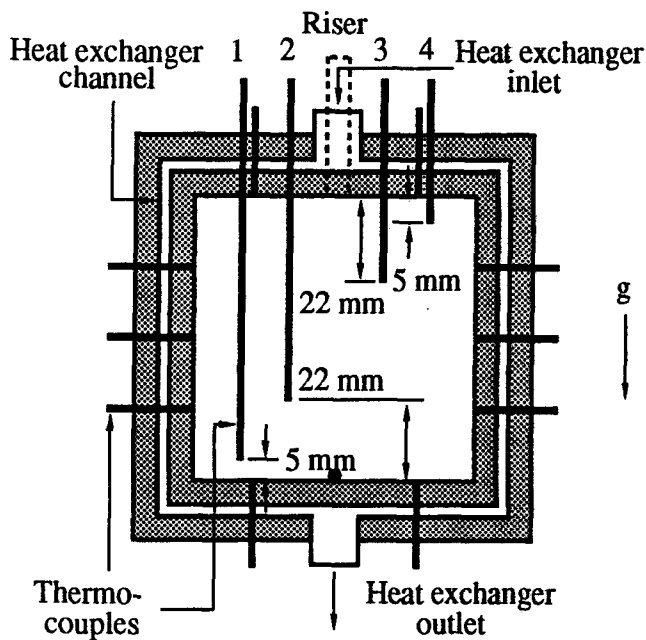
ent article, therefore, is to provide preliminary validation of the multiphase model through comparisons with carefully designed aqueous ammonium chloride equiaxed solidification experiments.

As a transparent analog for metallic alloys, the  $\text{NH}_4\text{Cl-H}_2\text{O}$  solution has been extensively used to study thermo-solutal convection during columnar solidification. Notable work includes that by Beckermann and Viskanta,<sup>[4]</sup> Christenson and Incropera,<sup>[5]</sup> Chen and Chen,<sup>[6]</sup> McCay *et al.*,<sup>[7]</sup> Neilson and Incropera,<sup>[8]</sup> and Magirl and Incropera.<sup>[9]</sup> In contrast, there exist relatively few experimental studies of equiaxed solidification using  $\text{NH}_4\text{Cl-H}_2\text{O}$ . The aqueous solution was used to visualize the qualitative features of equiaxed solidification in low gravity environments,<sup>[10,11]</sup> and quantitative measurements combined with visualization of two-dimensional (2-D) equiaxed dendritic solidification of an  $\text{NH}_4\text{Cl-H}_2\text{O}$  mixture were recently obtained by Beckermann *et al.*<sup>[12]</sup> A number of interesting characteristics of the solidification process were found, which include nucleation, fragmentation, recalescence, multicellular thermosolutal convection, and the sedimentation of  $\text{NH}_4\text{Cl}$  crystals.

In the present article, a combined experimental and numerical investigation is reported of equiaxed dendritic solidification of an  $\text{NH}_4\text{Cl-H}_2\text{O}$  solution in a square cavity evenly cooled from the sidewalls. The transparent alloy allows visualization not only of the solid-liquid multiphase transport phenomena but also the interactions of these flows with grain nucleation and growth kinetics, thus yielding a better understanding of the processes leading to structural and chemical inhomogeneities on the system scale. In parallel with the experimental program, numerical simulation of the solidification process, using the experimental conditions as input, is carried out using the multiphase model developed in part I and the numerical algorithm proposed in part II. The emphasis of the present article is on quantitative comparisons between the measurements and predictions.

C. BECKERMANN, Associate Professor, is with the Department of Mechanical Engineering, The University of Iowa, Iowa City, IA 52242. C.Y. WANG, Assistant Professor, is with the Department of Mechanical Engineering, University of Hawaii at Manoa, Honolulu, HI 96822.

Manuscript submitted February 9, 1995.



### • location of the out-wall thermocouple

Fig. 1—Schematic of the test cell and thermocouple locations.

## II. EXPERIMENTAL PROCEDURE

The experiments were performed in an enclosed square test cell made of a clear polycarbonate (Lexan), with inner dimensions 7.62-cm wide by 7.62-cm high by 5.08-cm deep (Figure 1). A riser was attached to the top of the test section, through which the test material was poured into the cavity before each experiment and continued to be slowly supplied during the experiment to compensate for solidification shrinkage.

The four sidewalls of the cell (left, right, top, and bottom) were rendered isothermal by the use of a heat exchanger in which a temperature-regulated coolant was circulated. The front and back walls were well insulated, with the insulation briefly removed to visualize flow conditions using a shadowgraph system (to visualize density gradients) or to observe the crystal shape and structure *via* normal photography. The insulation of the front and back surfaces of the cell resulted in primarily 2-D solidification behaviors.

In the shadowgraph setup, the light source consisted of a diverging beam from a mercury arc lamp which was collimated by reflecting it off a parabolic mirror. After passing through the test cell, the light was imaged on a translucent glass plate and photographed using Kodak\* Tmax 100 film.

\*KODAK is a trademark of Eastman Kodak Corporation, Rochester, NY.

Temperature measurements in the test apparatus were made using copper-constantan thermocouples, calibrated to an accuracy of  $\pm 0.1$  °C. Four thermocouples enclosed inside 1.8-mm-diameter stainless-steel tubes were inserted into the melt in the middepth plane and at the locations shown in Figure 1. Their horizontal locations were 12.7 and 25.4 mm, respectively, from each vertical sidewall of the inner cell. The other ten thermocouples were routed through

the heat exchanger channels and mounted close to the inner surfaces of the cell in an attempt to measure the temperatures along the four boundaries. Since the thermal boundary conditions represent important input to the computer simulation, extreme care was exercised to ascertain whether the wall temperatures are accurately represented by these ten in-wall thermocouples. For this purpose, a pure water cooling experiment was conducted in which a probe containing three thermocouples, in addition to the 14 others, was installed along the centerline of the test cell. The first thermocouple on the probe was tightly pressed onto the bottom inner surface of the test cell to provide another estimate of the wall temperature (called out-wall thermocouple for abbreviation). The other two thermocouples on the probe were located at  $y = 3.81$  and  $7.12$  cm from the bottom, respectively, for the measurement of interior temperature variations during the experiment. The experimental data for cooling of pure water will be presented in Section III-A along with the corresponding simulation results for the single-phase natural convection problem, in order to calibrate the wall temperature measurement.

For the solidification experiments, an aqueous solution of 30 wt pct  $\text{NH}_4\text{Cl}$  was chosen, and the initial temperature was kept at  $33.8$  °C, slightly above the equilibrium liquidus temperature ( $\sim 33.3$  °C). Before each experiment, the test cell was left idle for about 3 hours to reach equilibrium. Although a number of solidification experiments with different cooling rates have been performed, only one representative experiment is reported here and compared to the computed results. In this experiment, cooling was provided by impulsively switching the circulation loop encompassing the test cell to a second constant temperature bath set at  $2$  °C, which results in an average cooling rate of the order of  $1$  °C/min. The experiment (as well as the simulation) was terminated after about 15 minutes, at which point almost the entire cavity was occupied by crystals and no more observations of the flow were possible. The temperature measurement and visualization experiments were conducted separately so as not to interfere with each other. More details on the experimental procedures can be found in Reference 12, which also shows the phase diagram for the  $\text{NH}_4\text{Cl-H}_2\text{O}$  system.

## III. NUMERICAL MODEL

Assuming symmetry, the experimental system can be modeled as a 2-D cavity, 7.62 cm in height and 3.81 cm in width (*i.e.*, the half test cell). The mathematical formulation along with the numerical procedures, as presented in part II, is applied to simulate the  $\text{NH}_4\text{Cl-H}_2\text{O}$  solidification. Without repeating the details for brevity, several issues pertinent to the simulation of the  $\text{NH}_4\text{Cl-H}_2\text{O}$  experiment should be mentioned. First, the exact mechanisms and rates of grain generation in the  $\text{NH}_4\text{Cl-H}_2\text{O}$  system are presently not known. Therefore, it was decided to still use the instantaneous nucleation model, as presented in part I. The nucleation rate constant,  $n_0$ , was estimated to be roughly  $10^9$   $\text{m}^{-3}$ , which corresponds to an average grain size of 1.25 mm (if all crystals survive and grow to the same size). This value was estimated from the average crystal size observed during the experiment (discussed subsequently). Second, the dendrite tip growth law for  $\text{NH}_4\text{Cl}$  crystals may signif-

icantly differ from that for metallic alloys. However, due to a lack of data, the form of the growth law (*i.e.*, Stokes' solution) presented in part I for metal alloys was still employed in the present simulation of the  $\text{NH}_4\text{Cl-H}_2\text{O}$  experiment, except that the Gibbs-Thomson coefficient,  $\Gamma$ , was adjusted to yield an internal solid fraction of around 5 pct on average for the growing equiaxed dendritic crystals before grain impingement (discussed subsequently). This surprisingly low internal solid fraction has been widely reported in the literature for free-growing  $\text{NH}_4\text{Cl}$  crystals.<sup>[13,14]</sup> After several trial-and-error processes, the value of  $\Gamma$  was determined to be equal to  $5 \times 10^{-8}$  (mK), as listed in Table I. At present, neither the accuracy of the growth law nor the exact value of  $\Gamma$  for  $\text{NH}_4\text{Cl}$  is known.

Other thermodynamic properties and empirical constants used in the simulation are summarized in Table I. Note that the density of the solid  $\text{NH}_4\text{Cl}$  in the buoyancy term is roughly 50 pct larger than the liquid density. Hence, crystal sedimentation can be quite significant in the present system. The liquid density in the buoyancy term shown in Table I is a function of both temperature and liquid concentration, implying that thermosolutal convection in the liquid melt is fully taken into account. The linear liquidus line given in Table I was determined from the data in Reference 15, which covered the concentration range between 23 and 35 wt pct  $\text{NH}_4\text{Cl}$  or, equivalently, the temperature range between 0 °C and 50 °C, which is the range of the present experimental system. Last, the value of the secondary dendrite arm spacing was taken from the measurement made by Ahuja<sup>[14]</sup> with comparable cooling rates.

#### A. Thermal Boundary Conditions

The initial and boundary conditions are as follows: the cavity initially contains a quiescent  $\text{NH}_4\text{Cl-70}$  wt pct  $\text{H}_2\text{O}$  solution at a temperature of 307 K (about 0.3 K above the initial liquidus temperature). During solidification, the left, right, upper, and lower walls are impermeable and at a uniform, yet time-dependent temperature, which is obtained from the experimental measurement described subsequently. The velocity boundary conditions are the same as in part II.

As explained earlier, the ten in-wall thermocouples (embedded inside the walls of the test cell) and one out-wall thermocouple (touching the bottom from the inside of the test cell) were used to determine the average cell wall temperature variation. Figure 2 shows these temperature as functions of time. In addition, two interior temperatures, for  $y = 3.81$  and  $7.12$  cm along the centerline, are also included in the figure. Since the ten in-wall thermocouples, located at different positions around the boundaries, yielded readings differing by less than  $\pm 2$  °C, which was deemed small compared to the temperature difference between the wall and the melt (as high as 15 °C), only their average value is plotted in Figure 2. As can be seen from Figure 2, a significant discrepancy exists between the average in-wall temperature and the out-wall temperature, indicating a great uncertainty in the measurement of the wall temperature.

To remove this uncertainty, separate numerical simulations of the single-phase natural convection cooling experiment (discussed previously) were carried out using each wall temperature as the thermal boundary condition. It was found that the out-wall temperature measurement better

represents the actual wall temperature than the in-wall thermocouples. This is because the predicted interior temperatures using the out-wall temperature as the thermal boundary condition are in reasonable agreement with the experimental results, as shown in Figure 3. In general, the interior temperatures are somewhat overpredicted during the early stages of cooling, but become underpredicted by approximately 2.5 °C later in the experiment. Some of the discrepancy may be due to heat transfer between the test cell and the surroundings, which switches direction at room temperature ( $\sim 25$  °C). Using the in-wall temperature as the thermal boundary condition, however, would lead to intolerable underpredictions of the interior temperatures, since the in-wall temperature is much lower than the out-wall temperature. Of course, the validity of such a calibration is based on the assumption that the computer simulation realistically predicts the simple single-phase natural convection patterns inside the cell, which is likely the case. Therefore, the temperature measurement made by the out-wall thermocouple was determined to be a realistic boundary condition. For computational convenience, the measured wall temperature,  $T_w$ , was approximated by the following temporal function:

$$T_w(t) = 306.45 - 24(1 - e^{-0.0012t}) \quad [1]$$

where the time  $t$  is in seconds and  $T_w$  is in degree Celsius. The good agreement of this function with the actual measurement data can be seen from Figure 3.

The same cooling practice was used in both the pure water and the solidification experiments, namely, switching the cooling loop to a second circulator at a constant temperature of 2 °C at the beginning of each experiment. It was found that there existed no appreciable differences in the measured wall temperature histories between the two experiments. This is expected because the wall temperature is predominantly controlled by the thermal mass of the walls of the test cell, and the cooling conditions in the heat exchanger do not change. Therefore, Eq. [1] represents the thermal boundary condition for the solidification experiment as well.

#### B. Computational Details

The model equations presented in part II were solved using the same algorithm developed therein. A uniform  $40 \times 40$  grid was chosen for the half of the test cell simulated. It was found in other studies (*e.g.*, Reference 16) that similar grids are adequate for capturing the principal flow and solidification features at a reasonable computational cost. A time-step of 0.1 seconds was employed for the first 400 seconds and doubled during the later stages of the simulation. Each 1 second of real-time simulation required approximately 120 CPU seconds on an IBM\* 3090 computer.

---

\*IBM is a trademark of International Business Machines Corp., Armonk, NY.

## IV. RESULTS AND DISCUSSION

In this section, both experimental and numerical results are reported for the equiaxed dendritic solidification of an  $\text{NH}_4\text{Cl-70}$  wt pct  $\text{H}_2\text{O}$  solution. Comparisons are made be-

**Table I. Thermophysical Properties and System Data for NH<sub>4</sub>Cl-70 Wt Pct H<sub>2</sub>O Alloy**

Properties (Unit)	Value
Cavity dimensions $H \times L$ (cm $\times$ cm)	7.62 $\times$ 7.62
<b>Initial and Boundary Data</b>	
Initial temperature of the liquid melt, $T_m$ (K)	307
Initial concentration, $C_m$ (wt pct H <sub>2</sub> O)	70
Wall temperature function, $T_w(t)$ (K)	$306.45 + 24(e^{-0.072t} - 1)$
<b>Property Data<sup>[12]</sup></b>	
Density of the liquid phase, $\rho_l$ (kg/m <sup>3</sup> ) (except in buoyancy term)	1078
Density of the solid phase, $\rho_s$ (kg/m <sup>3</sup> ) (except in buoyancy term)	1078
Density of the liquid phase in buoyancy term (kg/m <sup>3</sup> ) ( $T$ in K; $C_l$ in wt pct H <sub>2</sub> O)	$1078[1 - 3.23 \times 10^{-4}(T - T_m) - 3.65 \times 10^{-4}(C_l - C_m)]$
Density of the solid phase in buoyancy term (kg/m <sup>3</sup> )	1527
Dynamic viscosity of the liquid phase, $\mu_l$ (N s/m <sup>2</sup> )	0.0013
Thermal conductivity of the liquid phase, $k_l$ (W/m K)	0.468
Thermal conductivity of the solid phase, $k_s$ (W/m K)	2.7
Specific heat of the liquid phase, $c_l$ (J/kg K)	3249
Specific heat of the solid phase, $c_s$ (J/kg K)	1827
Latent heat of fusion at $T_E$ , $\Delta h$ (J/kg)	$3.138 \times 10^5$
Mass diffusivity of the liquid phase, $D_l$ (m <sup>2</sup> /s)	$4.8 \times 10^{-9}$
Mass diffusivity of the solid phase, $D_s$ (m <sup>2</sup> /s)	0
Segregation coefficient, $\kappa$ (wt pct/wt pct)	0.003
Eutectic concentration, $C_E$ (wt pct H <sub>2</sub> O)	80.3
Eutectic temperature, $T_E$ (K)	259.2
Liquidus temperature, $T_L$ (K) ( $C_l$ in wt pct H <sub>2</sub> O)	$629.403 - 4.61 C_l$
Gibbs-Thomson coefficient, $\Gamma$ (m K) (adjusted)	$5 \times 10^{-8}$
<b>Empirical Constants</b>	
Maximum grain packing fraction, $\epsilon_g^c$	0.637
Initial grain diameter, $d_{si}$ ( $\mu$ m)	1
secondary dendrite arm spacing, $\lambda_2$ ( $\mu$ m)	75

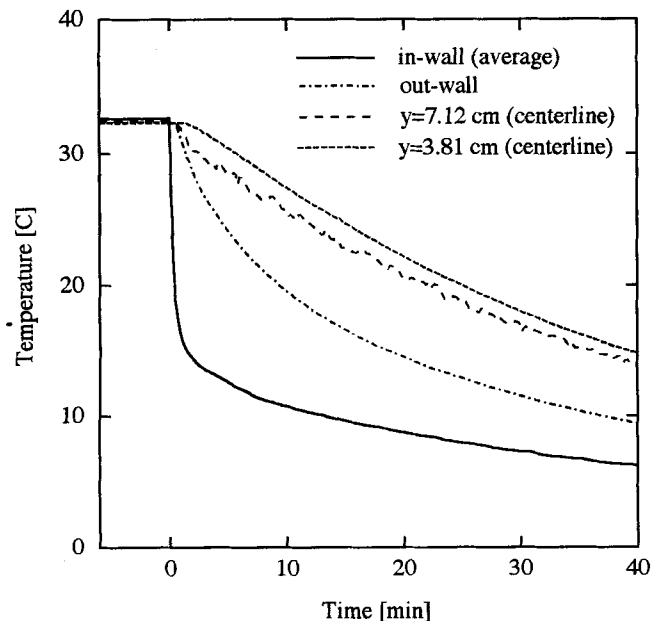


Fig. 2—Temperature histories for the pure water experiment.

tween the numerical predictions and experimental data in terms of the evolution of the bed of sedimented crystals (Figures 4 through 6) and cooling curves (Figure 11).

#### A. Sediment Bed

Selected shadowgraph images of the solidification process at various times are displayed in Figures 4(a), 5(a),

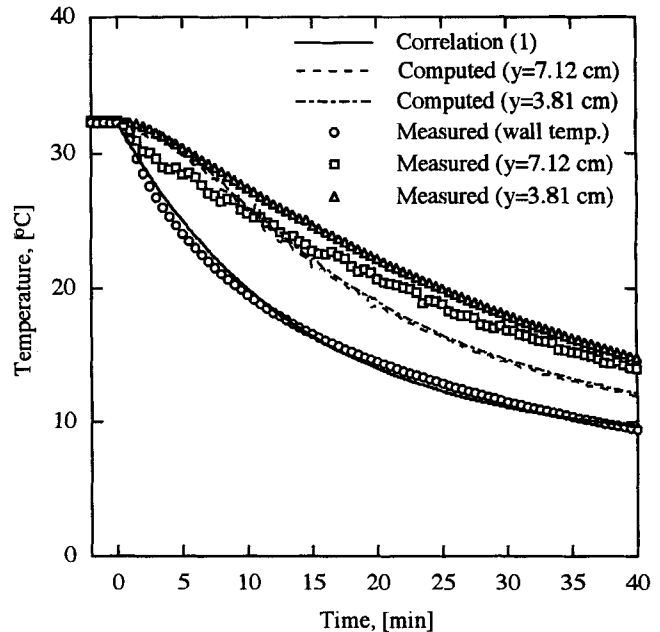
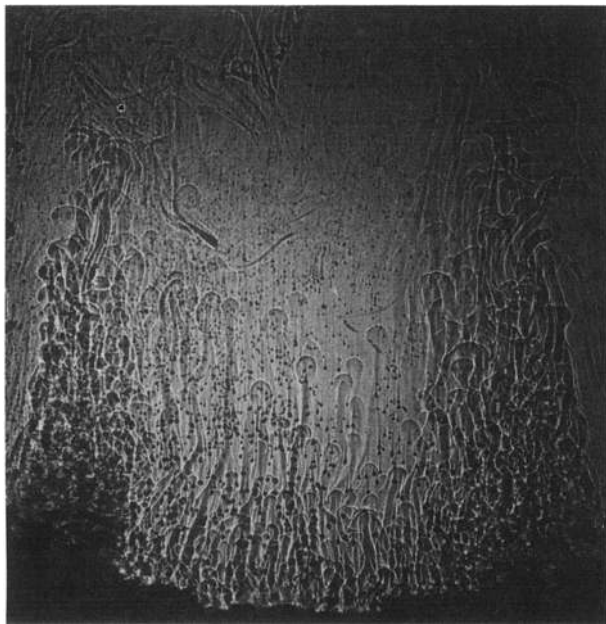
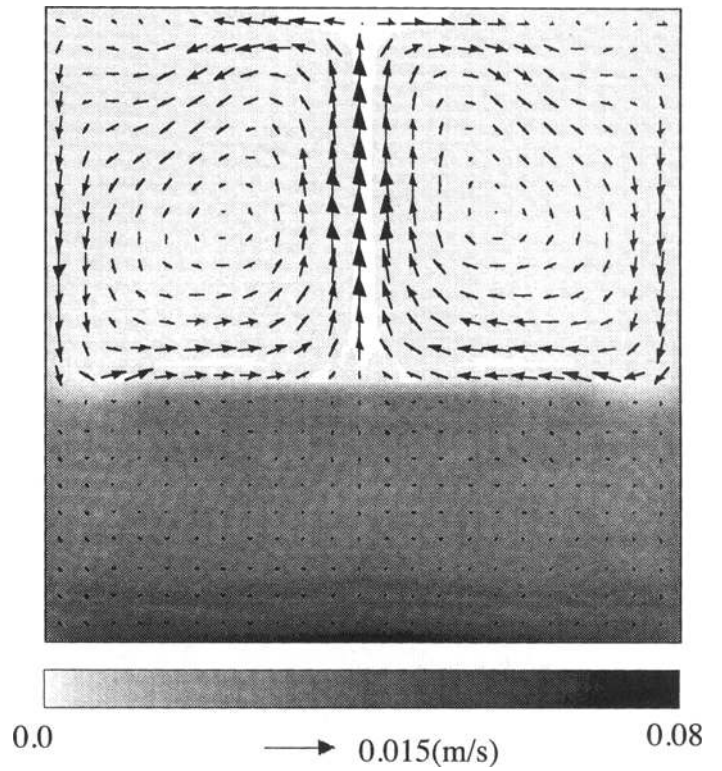


Fig. 3—Comparison of measured and predicted temperatures for the pure water experiment.

and 6(a). Because the cold wall was always kept above the eutectic temperature, no pure solid zone developed in the test cell. It should also be mentioned that the fine microstructure of the equiaxed grains is not visible in the images obtained using the shadowgraph system. Instead, normal

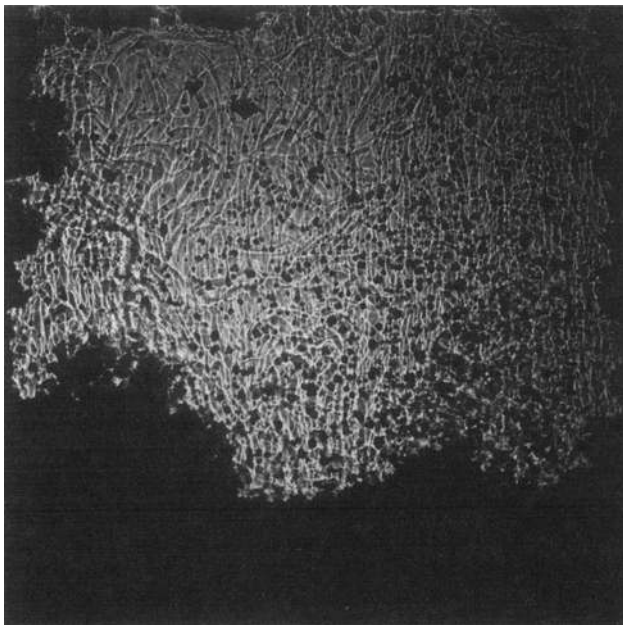


(a)

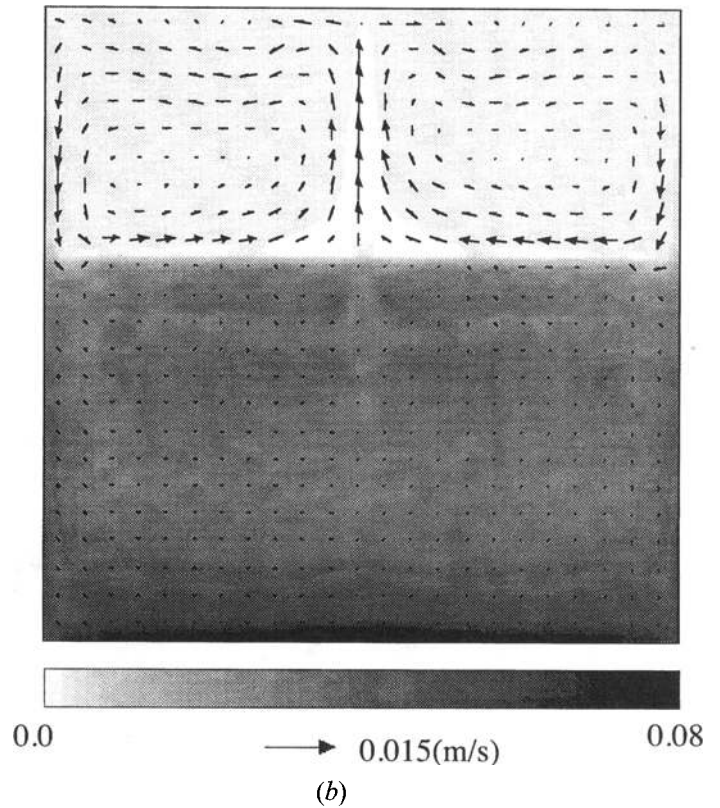


(b)

Fig. 4—Comparison of measured and predicted results at  $t = 450$  s: (a) shadowgraph image and (b) solid volume fraction and liquid velocity fields.



(a)

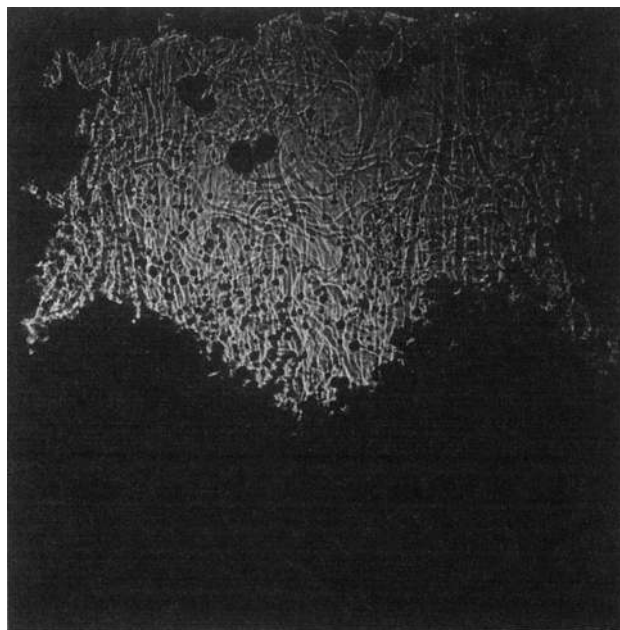


(b)

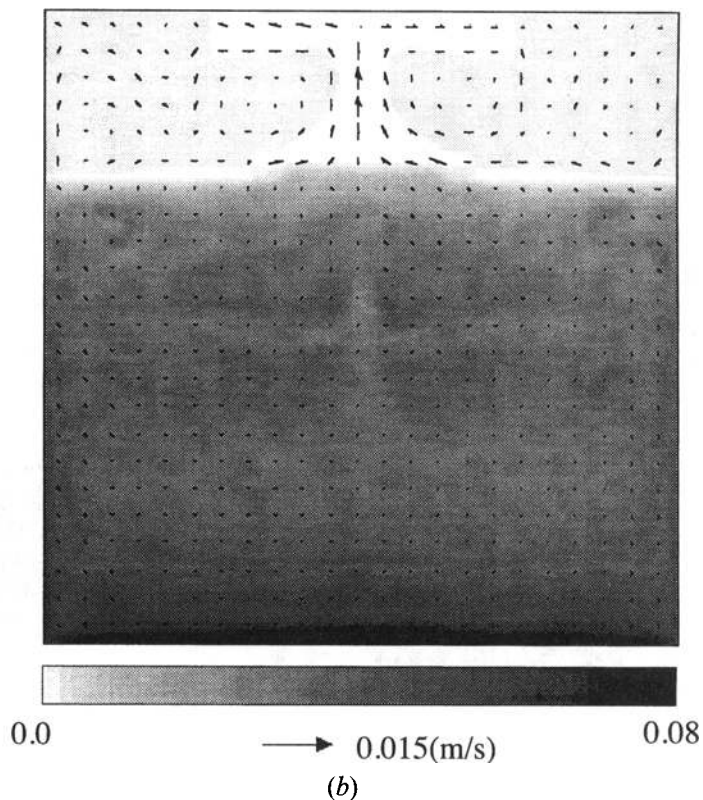
Fig. 5—Comparison of measured and predicted results at  $t = 645$  s: (a) shadowgraph image and (b) solid volume fraction and liquid velocity fields.

photography was used to observe the dendritic structure (Figure 10).

Upon initiation of cooling, a certain undercooling is es-



(a)



(b)

Fig. 6—Comparison of measured and predicted results at  $t = 765$  s: (a) shadowgraph image and (b) solid volume fraction and liquid velocity fields.

tablished in the liquid, and the solid begins to nucleate first at the walls where the temperature is the lowest. At about 360 seconds into the experiment, a large number of free grains was observed in the upper portion of the melt. Based on our observations, they originate from fragmentation of the crystals at the walls and are advected into the bulk melt by the flow. The free crystals continue to grow in the undercooled liquid and tend to settle down due to the solid being much heavier than the liquid melt. This can be clearly observed in Figures 4(a) at  $t = 450$  seconds. The crystals finally settle toward the floor of the test cell and form a sediment bed. According to the phase diagram, the forming solid is almost pure  $\text{NH}_4\text{Cl}$  and, thus, water is rejected from the crystals to the immediately surrounding liquid. The  $\text{H}_2\text{O}$ -rich liquid forms solutal wakes behind each crystal as it travels through the liquid melt. Due to the low liquid mass diffusivity, these wakes retain their composition identity and are clearly visible in the shadowgraph image shown in Figure 4(a). On the system scale, the  $\text{H}_2\text{O}$ -rich, lighter liquid rejected from the crystal sediment bed rises up through the surrounding liquid in the form of relatively large fingers, which can also be seen in Figure 4(a). This fingering of water-rich liquid is sustained by the continued solidification of crystals that settled at the bottom of the cell. In the regions adjacent to the two vertical sidewalls, a downward flow develops due to the cooling effect. Figure 4(a) reveals the presence of boundary layers adjacent to the left and right sidewalls. The downward thermal buoyancy forces near the sidewalls oppose the upward solutal buoyancy forces, thereby causing a deflection of the  $\text{H}_2\text{O}$ -rich fingers as they ascend upward. Upon further cooling, the

sediment bed continues to increase in height while keeping an irregular shape, as can be seen from Figure 5(a). At  $t = 750$  seconds more than half of the test cell is filled with a mush of settled equiaxed crystals (Figure 6(a)).

Throughout the experiment, only little growth was observed along the side and top walls above the sediment bed, although cooling was uniform from all sides. In fact, Figures 4(a) through 6(a) give the appearance of unidirectional solidification from bottom to top. Again, this appearance is caused by the setting of the crystals toward the bottom. The solid fraction in the upper portion of the cavity remains low, because solidification is not fast enough to compensate for the settling of the crystals out of this region. Once the crystals have settled, they cannot increase in size due to the packing effect in the sediment bed.

As discussed previously, a distinctive feature of the present equiaxed solidification experiment is the formation of a crystal sediment bed, as a direct result of crystal sedimentation. The evolution of the size and shape of the bed is determined by many factors including the following: (1) the crystal size which is mainly controlled by the generation rates and growth rates of the equiaxed crystals; (2) the solid/liquid interfacial drag which directly dictates the sedimentation rate; and (3) the convective flow patterns in the liquid melt. Each of these factors is further related to a number of fundamental, but yet to be addressed, issues, including the grain nucleation and fragmentation mechanisms in the presence of convective flow, grain growth with relative melt motion, and thermosolutal convection in a melt laden with solid crystals. Although it may seem premature to make comparisons between the measured and

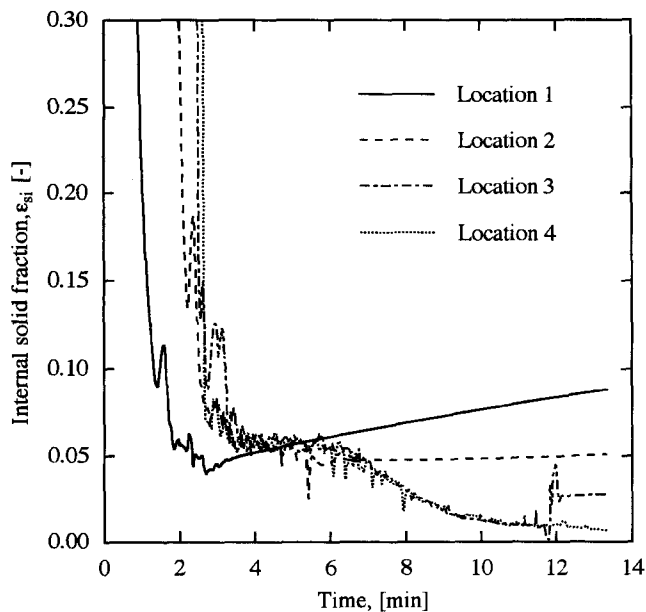


Fig. 7—Evolution of the internal solid fraction as predicted from the numerical model.

simulated results for the evolution of the sediment bed, such an attempt is made subsequently in order to provide preliminary model validation and, more importantly, to identify the critical areas where more future research is required.

Figures 4(b), 5(b), and 6(b) show the predicted results for the solid fraction distribution at the same times as the experimental shadow graph images in panels (a). The computed solid fraction images are superimposed by the liquid velocity vectors. Display of the numerical results in the entire cavity was made possible by duplicating the numerical solution for one half to the other half assuming symmetry.

The predicted results in Figures 4(b) through 6(b) show that the crystal sediment bed is characterized by a relatively low solid fraction throughout the settling process, because the  $\text{NH}_4\text{Cl}$  crystals are highly dendritic. To illustrate this, the computed evolution of the internal solid fraction is displayed in Figure 7 at the same four locations as the thermocouples shown in Figure 1. The internal solid fraction is defined as the ratio of the solid fraction to the grain fraction. The lower the internal solid fraction, the more dendritic an equiaxed crystal is. An internal solid fraction of unity corresponds to a globulitic crystal. It can be seen from Figure 7 that within the first 3 minutes, the internal solid fraction at all locations decreases in an abrupt and oscillatory fashion. This first stage corresponds to the change from a globular nucleus upon nucleation to a fully dendritic crystal grown freely in the undercooled melt. Later, the internal solid fraction at the lowest position (location 1) gradually and smoothly increases. This increase is characteristic of the slow thickening of the dendrite arms inside a stationary crystal within the sediment bed (after impingement). At location 2, the internal solid fraction stays approximately constant at 5 pct, since the thickening of the arms is delayed at more internal locations. In the upper portion of the cavity (locations 3 and 4), the internal solid fraction continues to evolve in an oscillatory fashion in the interval between 0 and 5 pct. These oscillations, as well as the ones at all locations at earlier times, can be attributed to the highly

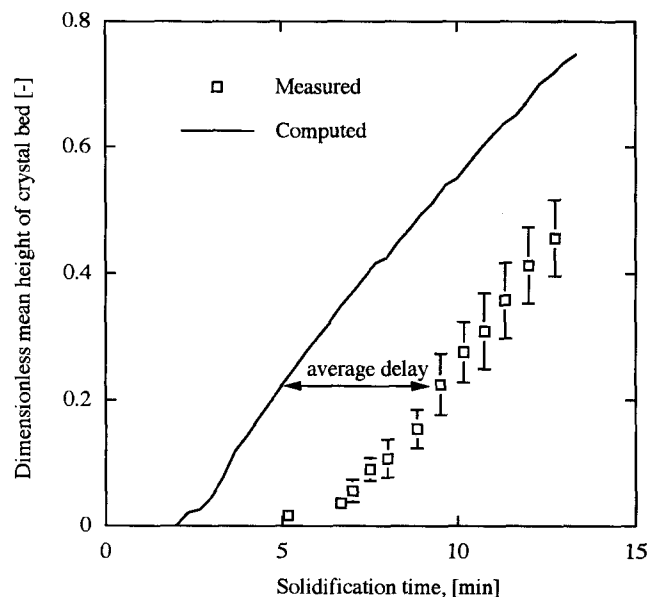


Fig. 8—Comparison of measured and predicted evolutions of the mean height of the crystal sediment bed.

transient growth and movement of free equiaxed crystals and thermosolutal convection patterns (discussed further in Section IV-B). The oscillations disappear as soon as the crystals pack to form the stationary sediment bed. The oscillations at locations 3 and 4 persist for a longer time, because packing of the grains occurs later in the upper portion. In fact, the last oscillation of the internal solid fraction for location 3 occurs at approximately 12 minutes, marking the point in time at which the sediment bed has increased to the height corresponding to this location (Figure 8). The relatively low value of the internal solid fraction after the initial growth stage observed in Figure 7 (about 5 pct) is in agreement with other measurements in the  $\text{NH}_4\text{Cl-H}_2\text{O}$  system for single dendrites<sup>[13,14]</sup> as well as for *in situ* crystallization.<sup>[13]</sup> Recall that this value of the internal solid fraction was produced by adjusting the growth kinetic parameter,  $\Gamma$ , in the present numerical model. The 5 pct average internal solid fraction for free equiaxed crystals combined with the packing limit for the grain fraction (preset at 0.637) implies that the edges of the sediment beds in Figures 4(b) through 6(b) correspond to a solid fraction of around 3 pct. The oscillatory nature of the internal solid fraction, which can be observed in Figure 7, can be attributed to grain movement.

Referring back to Figures 4 through 6, the predicted and measured sediment beds are seen to considerably differ from each other in both extent and shape. To uncover the possible factors responsible for these discrepancies, the extent and shape of the sediment bed are analyzed separately. Figure 8 compares the predicted and measured average heights (dimensionless) of the crystal sediment bed. As can be seen, there exists a delay of approximately 4 minutes in the experimental height. However, the model appears to be able to reproduce the experimental growth rate of the crystal sediment bed. The delay may be attributed to the dendrite fragmentation observed during the early stages of the experiment. Fragmentation needs some time to establish itself as a grain generation mechanism, because, first, some crystals need to nucleate and grow at the walls, then the

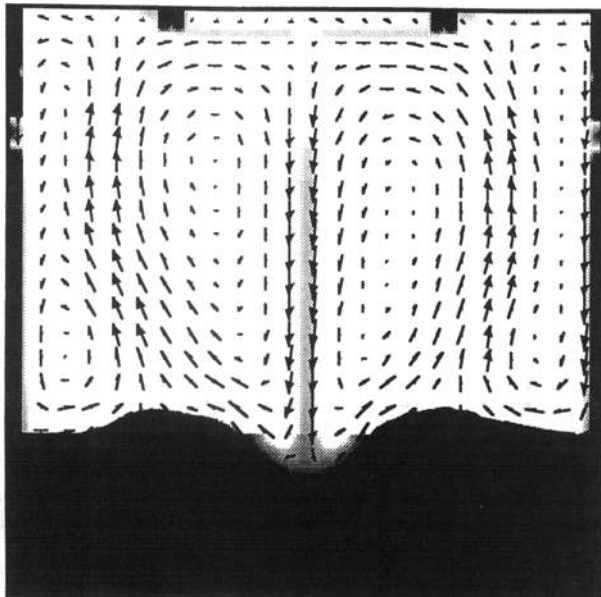


Fig. 9—Predicted solid volume fraction and liquid velocity fields for a higher cooling rate at  $t = 240$  s.

dendrite arms need to become unattached, and finally the convective current needs to carry the dendrite fragments into the bulk melt. On the other hand, in the model, it is assumed that nucleation occurs instantaneously as soon as the melt locally reaches the liquidus temperature. It would have been easy to implement such a delay in the present nucleation model, but it was felt that any modification should await the development of a realistic fragmentation model.

Beckermann *et al.*<sup>[12]</sup> postulated that the curved shape of the sediment bed is largely caused by the thermosolutal convection patterns in the liquid melt above it. As shown in Figures 4(b) through 6(b), two convection cells are predicted to exist in the upper melt. At the vertical sidewalls, the downward thermal buoyancy forces are dominant over the solutal ones, while the two augment each other near the cell center. These convective cells play an important role in the transport of the solid phase: the movement of the smallest crystals closely follows the motion of the liquid due to the large interfacial drag. However, it is evident from Figures 4(b) through 6(b) that the predicted thermosolutal convection flow is not strong enough to effectively promote a curved shape of the sediment bed. To delineate the underlying mechanisms for an irregular crystal sediment bed, an additional numerical simulation was performed in which the wall temperature was replaced by

$$T_w(t) = 306.45 - 24(1 - e^{-0.0017t}) \quad [2]$$

while all the other conditions and parameters remained the same. The average cooling rate in this illustrative case is increased by about 40 pct compared to the experiment. As shown in Figure 9, a completely different flow pattern appears in this higher cooling rate case when compared, for example, to Figure 4(b). The flow above the sediment bed consists of four cells, with the flow being downward along the centerline. This multiplication of circulation cells results

5 mm

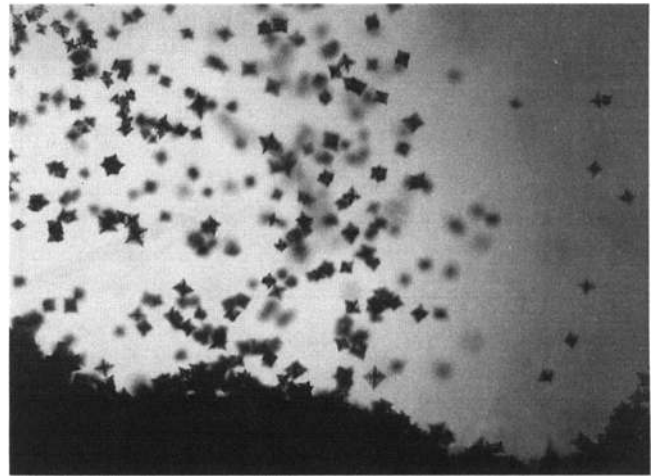


Fig. 10—Close-up of settling equiaxed crystals and the sediment bed.

directly from changing the cooling rate and, hence, enhancing the thermal buoyancy forces. At the vertical sidewalls, the liquid still descends due to the strong thermal buoyancy forces. At about a quarter width of the test cell from each of the two vertical walls, the warmer and  $H_2O$ -rich liquid forms a strong upward jet, which forces the liquid to descend at the center. The effect of this flow pattern on the shape of the sediment bed is apparent from Figure 9, where all regions with a solid fraction above 3 pct are displayed as a single color (*i.e.*, black) for clarity and for being directly comparable with the shadowgraph images. It can be seen that the descending liquid at the center causes a depression in the crystal sediment bed, whereas the upward flows near the middle of each half of the cavity lead to mounds at those locations. The appearance of the curved crystal sediment bed simulated for the case of a higher cooling rate is in reasonable agreement with the shadowgraph image shown in Figure 5(a). Although the hypothetical cooling rate results in an unrealistic temporal evolution, this illustrative simulation clearly provides evidence that the shape of the sediment bed is closely related to the thermosolutal convection patterns in the liquid above it. The fact that a low cooling rate produces a more uniform sediment bed is in agreement with the findings of Beckermann *et al.*<sup>[12]</sup> who performed experiments at two different cooling rates. In addition, it is interesting to note from Figure 9 that in the case of a higher cooling rate, some coherent dendrite network is predicted above the sediment bed along the two vertical sidewalls as well as at the upper wall, a feature that can also be observed in the experimental images. The coherent dendrite network forms along these walls, because the crystal growth in the high cooling rate simulation is fast enough for the crystals to pack before significant settling occurs. Nonetheless, the issue of sticking of dendrites to walls does deserve further research attention.

Overall, it can be said that the simulation successfully captures the growth rate of the sediment bed, leading to the following conclusions. First, the packing limit must definitely be based on the grain fraction instead of the solid fraction. If based on the solid fraction, no sediment bed would have been predicted throughout the solidification



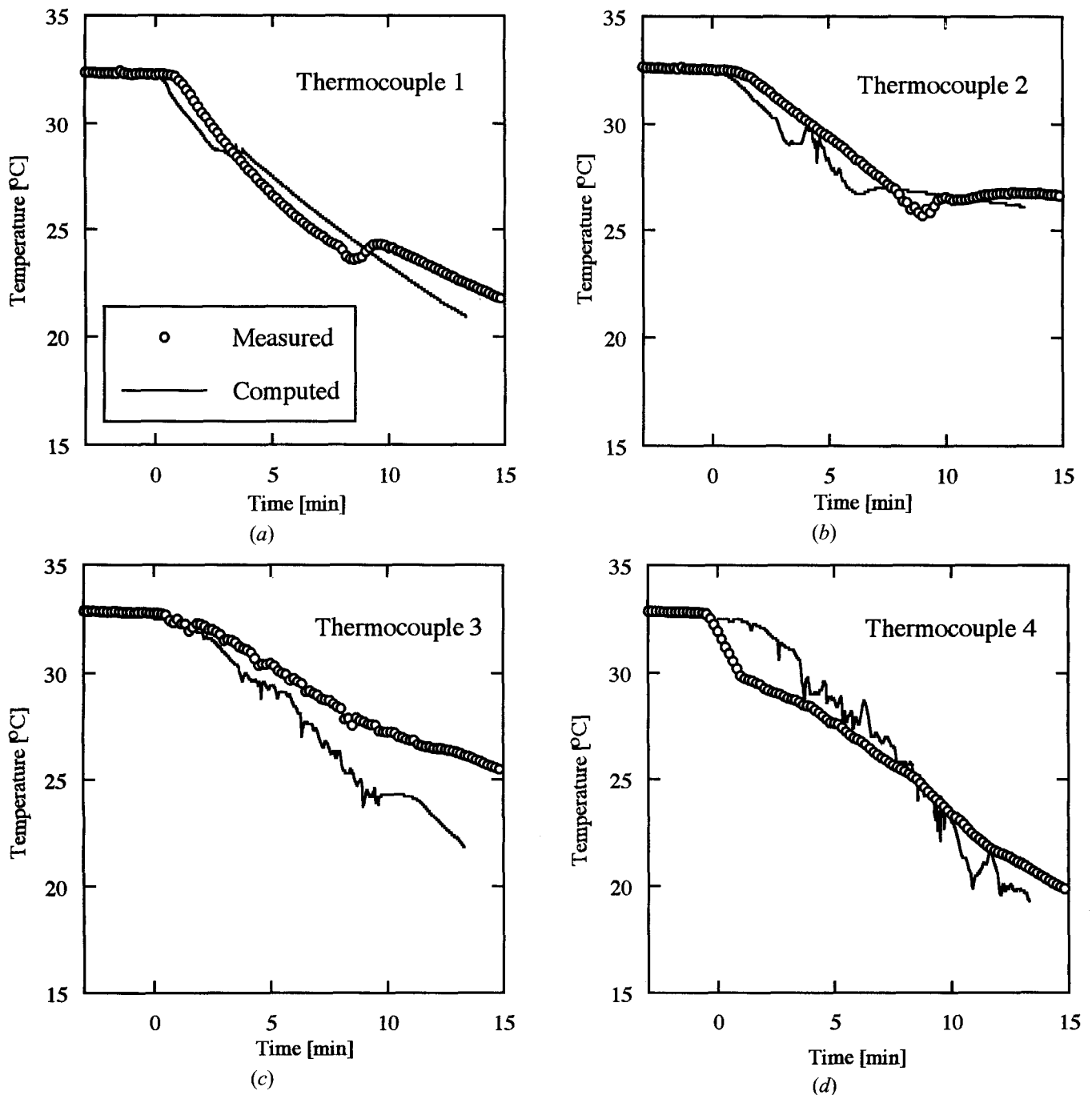


Fig. 11—Comparison of measured and predicted cooling curves: (a) thermocouple 1, (b) thermocouple 2, (c) thermocouple 3, and (d) thermocouple 4.

process, since the  $\text{NH}_4\text{Cl}$  crystals are highly dendritic. Second, the overall size of the falling crystals greatly influences the sedimentation rate. This is why the nucleation rate constant in the present simulation was carefully chosen so that the resulting free equiaxed crystals have an average size of about 1.25 mm in diameter just before impinging upon each other. A close-up of settling equiaxed crystals, from which their size can be measured, is provided in Figure 10. Finally, the sedimentation rate is also controlled by the solid/liquid interfacial drag, which has been the topic of a previous study by the present authors.<sup>[1]</sup> Considering the fact that globular crystals would have a much different set-

ting behavior than highly dendritic crystals of the  $\text{NH}_4\text{Cl}$ - $\text{H}_2\text{O}$  system, the present multiscale description of the interfacial drag can be considered essential.

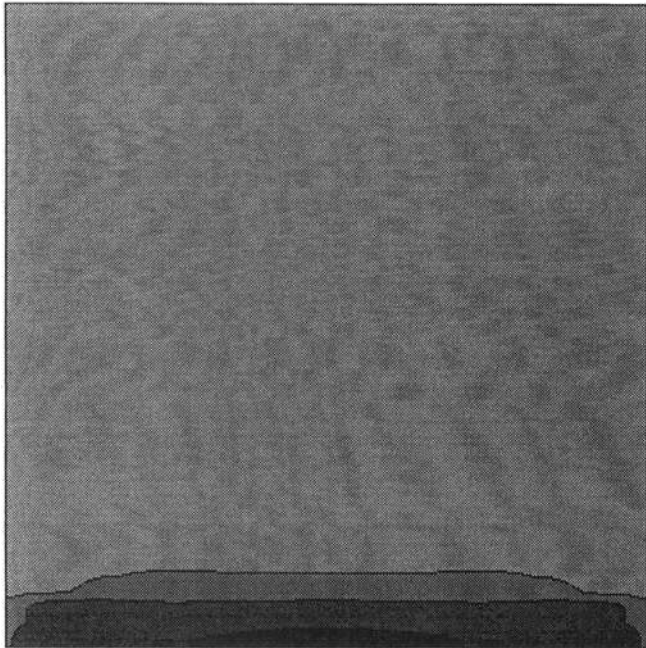
### B. Cooling Curves

Figure 11 shows a comparison of the measured and predicted cooling curves at the four interior locations shown in Figure 1. Overall, it can be seen from Figure 11 that the predicted cooling curves are in reasonable agreement with the experimental measurements. Both the predicted and measured cooling curves for locations 1 and 2 exhibit a pronounced recalescence. Neither in the experiment nor in the simulation are the recalescences at the two locations within the same temperature range (compare Figures 11(a)

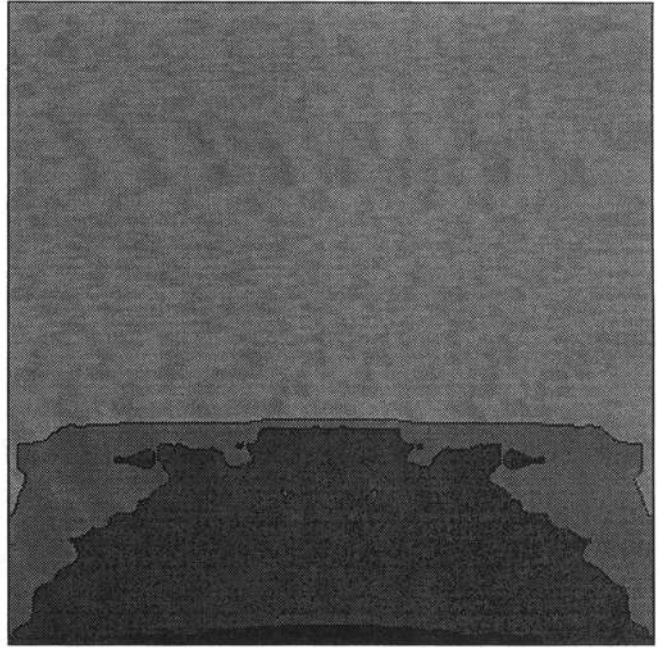
Mixture concentration in weight fraction H<sub>2</sub>O



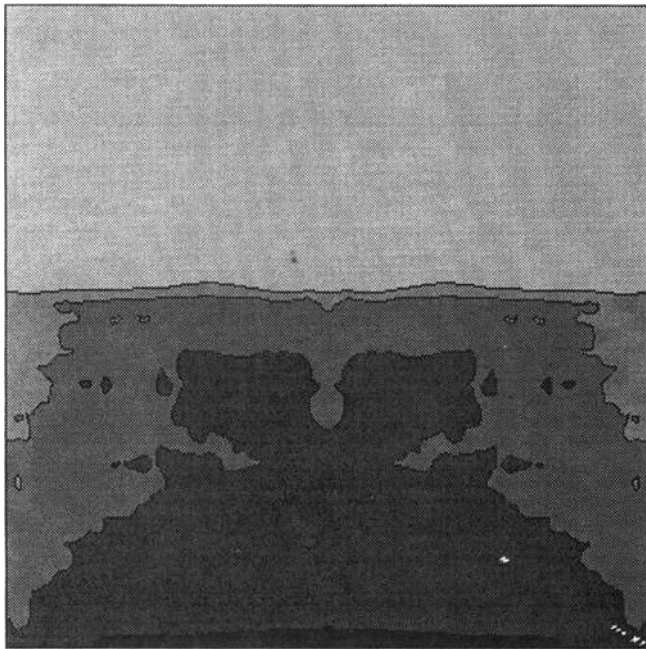
0.68 0.69 0.70 0.71 0.72



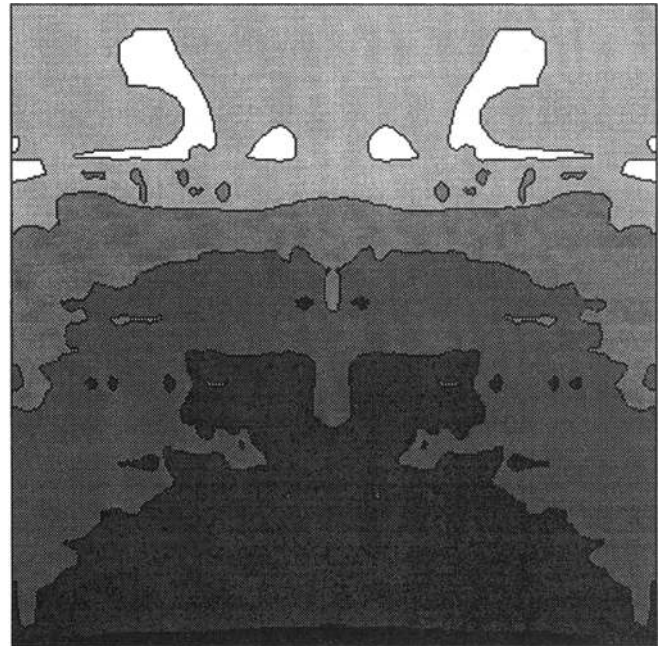
(a)



(b)



(c)



(d)

Fig. 12—Predicted macrosegregation patterns at (a) 200 s, (b) 400 s, (c) 600 s, and (d) 800 s.

and (b)). Through a comparison of Figures 11 and 8, it can be inferred that both the measured and predicted recalescences occur when the edge of the sediment bed passes by the thermocouple locations. In this comparison, it should be kept in mind that the measurements corresponding to Figures 11 and 8 were conducted in separate tests (under identical cooling conditions; discussed previously) and that the shape of the sediment bed was highly irregular. Typi-

cally, recalescence is closely associated with nucleation; however, this is unlikely to be the cause in the present system because of the presence of relatively large crystals near the sediment bed edge (Figure 10).

The measured and predicted recalescences in the present system may be explained as follows. Above the sediment bed, the (extradendritic) melt is in an undercooled state, as evidenced by the growth of the free crystals. Inside the

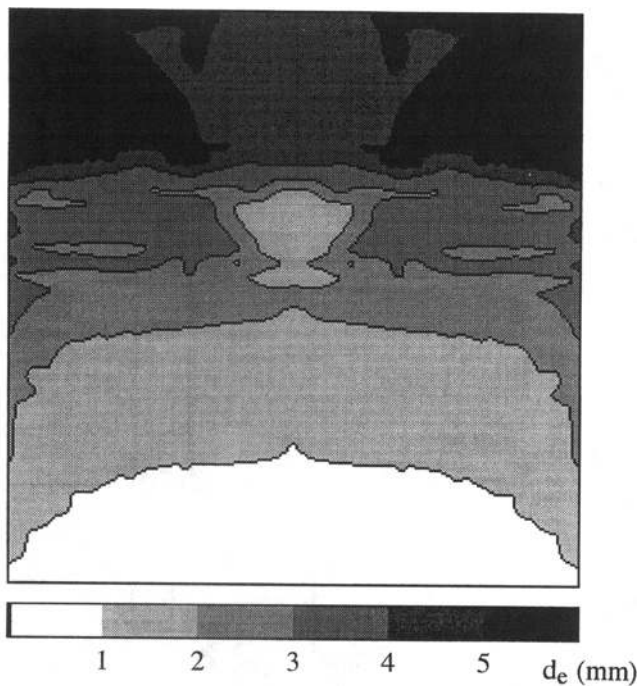


Fig. 13—Predicted grain diameter distribution at 800 s.

sediment bed, on the other hand, the melt, being confined to the interdendritic spaces, can be expected to be solutally well mixed and at a temperature corresponding to the local equilibrium liquidus concentration. Thus, as the crystals settle at the edge of the sediment bed, the system locally adjusts from an undercooled to an equilibrium state by raising its temperature (note that the concentration cannot adjust rapidly enough due to the low mass diffusivity). The measured temperature rise during the recalescences is roughly 1 °C, which therefore corresponds to the undercooling above the bed. Because the local concentrations continue to evolve due to convection (Figure 12), the recalescence temperatures are different at each location. The measured recalescences last for about 1 minute, during which time the sediment bed height increases by approximately 5 mm (Figure 8). Hence, in view of Figure 10, the adjustment from an undercooled to an equilibrium state at the sediment bed edge takes place over 3 to 5 crystal diameters. Compared with the predictions, the measured recalescences at locations 1 and 2 are delayed by exactly the same amount of time (about 4 minutes) as the measured sediment bed heights. The reason for the delay is the same as explained in connection with Figure 8 in Section A. Due to continued cooling of the system, the delay causes the measured recalescence temperatures to be lower than the predicted ones (Figures 11(a) and (b)).

The predicted cooling curves for the two locations in the upper melt (3 and 4), as well as to a lesser extent for locations 1 and 2, show relatively strong temperature fluctuations. The fluctuations occur only when the locations are above the sediment bed, and the predicted temperature histories become smooth after recalescence (e.g., Figure 11(c) after about 12 minutes). As mentioned previously in connection with Figure 7, the fluctuations are caused by the highly transient equiaxed crystal growth and movement and thermosolutal convection patterns prevailing above the sediment bed. Similar fluctuations have been predicted in other

highly accurate simulations of thermosolutal convection.<sup>[17,18]</sup> They have also been measured in other solidification experiments involving the  $\text{NH}_4\text{Cl-H}_2\text{O}$  system.<sup>[5,8,9]</sup> The only reason the fluctuations are not apparent in the present temperature measurements (although there is some evidence in Figure 11(c)) is that the data acquisition period was only 10 seconds.

### C. Predicted Macrosegregation Patterns and Grain Size Distribution

The evolution of macrosegregation is displayed in Figure 12 and can be explained by the countercurrent solid-liquid flow discussed in Section B. In Figure 12, macrosegregation is quantified in terms of the mixture concentration of  $\text{H}_2\text{O}$  defined as

$$C_{\text{mix}} = \varepsilon_s C_s + \varepsilon_f C_f \quad [3]$$

with the nominal composition being 70 wt pct  $\text{H}_2\text{O}$ . The solute-poor solid settles at the bottom to form the sediment bed, while the solute-rich, lighter liquid rises up in the form of fingers. As a result, a severe macrosegregation pattern develops. A bottom cone of negative segregation, which is generally believed to be caused by the sedimentation of solute-poor solid,<sup>[19]</sup> is indeed predicted by the present multiphase model.

Figure 13 shows the predicted grain size (diameter) distribution at 800 seconds. Without solid movement, the predicted grain diameter would be uniformly equal to 1.25 mm. The average value over the entire domain in the present case with grain transport is somewhat higher, which can only be explained by the death of grains due to complete remelting as a consequence of advection of grains into superheated regions at early times. The grain size increases strongly with vertical distance from the bottom wall. This is directly caused by the crystal settling, resulting in a high grain density in the lower regions at the expense of the upper part. Referring to Figure 10, which shows grains (with  $d_e < 2$  mm) in the lower part of the cavity (i.e., early into the experiment), as well as to Figure 6(a), which shows relatively large (attached) grains in the upper portion, the predicted vertical grain size variation from about 1 to 6 mm does not seem unrealistic. The predicted nonuniformities in the horizontal direction can be attributed to the bicellular convection pattern during solidification (as previously discussed).

Neither the final macrosegregation nor the grain size distributions can be easily compared with measurements when using transparent model alloys. Such comparisons for the case of a binary metallic alloy will be attempted in the near future.

## V. CONCLUSIONS

Equiaxed dendritic solidification of an aqueous ammonium chloride solution in a square cavity has been studied both experimentally and numerically. Solidification starts with crystal nucleation, fragmentation, and growth in the undercooled liquid melt. When the unattached crystals are still small, they closely follow the liquid flow, which is induced by both thermal and solutal buoyancy forces. After the crystals have grown to a certain size, they settle down

and form a sediment bed on the cavity floor. The  $\text{NH}_4\text{Cl}$  crystals are found to have an internal solid fraction of only about 5 pct at the point of grain impingement. This highly dendritic nature of the crystals complicates the solid-liquid multiphase flow occurring during solidification.

The solute-rich, lighter liquid rejected during solidification ascends in the form of fingers. The countercurrent liquid-solid multiphase flow is responsible for severe macrosegregation. The predicted bottom zone of negative segregation is directly caused by the sedimentation of solute-poor solid. Sedimentation is also responsible for a strong increase in the grain size with distance from the bottom.

Overall, the numerical simulation based on the multiphase model has reproduced some key features of the experiment, such as grain growth in the presence of grain movement, recalescence, and the rate of formation of the crystal sediment bed. The agreement with the experiment is reasonably good, considering that several gross simplifications have been made in the numerical model. Much better agreement seems likely if dendrite fragmentation is properly accounted for. Other issues that require an increased fundamental understanding include the effects of convection on free dendritic growth and the highly transient and three-dimensional thermosolutal convection patterns in the liquid. Some of the disagreement may also be attributed to an inaccurate knowledge of the thermal boundary conditions and thermophysical properties and to inaccuracies in the model equations and their solutions.

#### ACKNOWLEDGMENTS

This work was supported by the National Aeronautics and Space Administration under Grant No. NCC3-290. The authors thank Messrs. R.J. Feller and H. Müller-Späth for

assistance in performing the experiments and Mr. C. Fan for help with the numerical simulations.

#### REFERENCES

1. C.Y. Wang, S. Ahuja, C. Beckermann, and H.C. de Groh III: *Metall. Mater. Trans. B*, 1995, vol. 26B, pp. 111-19.
2. C.Y. Wang and C. Beckermann: *Metall. Mater. Trans. A*, 1996, vol. 27A, pp. 2754-64.
3. C.Y. Wang and C. Beckermann: *Metall. Mater. Trans. A*, 1996, vol. 27A, pp. 2765-83.
4. C. Beckermann and R. Viskanta: *PhysicoChem. Hydrodynamics*, 1988, vol. 10, pp. 195-213.
5. M.S. Christenson and F.P. Incropera: *Int. J. Heat Mass Transfer*, 1989, vol. 32, pp. 47-68.
6. C.F. Chen and F. Chen: *J. Fluid Mech.*, 1991, vol. 227, pp. 567-86.
7. M.H. McCay, T.D. McCay, and J.A. Hopkins: *Metall. Trans. B*, 1993, vol. 24B, pp. 669-75.
8. D.G. Neilson and F.P. Incropera: *Exper. Heat Transfer*, 1993, vol. 6, pp. 131-55.
9. C.S. Magirl and F.P. Incropera: *ASME J. Heat Transfer*, 1993, vol. 115, pp. 1036-43.
10. M.H. Johnston and P.A. Parr: *Materials Processing in the Reduced Gravity Environment of Space*, G.E. Rindone, ed., Materials Research Society, 1982, pp. 651-56.
11. J.M. Papazian and T.Z. Kattamis: *Metall. Trans. A*, 1980, vol. 11A, pp. 483-93.
12. C. Beckermann, R.J. Feller, T.R. Erwin, H. Müller-Späth, and C.Y. Wang: AIAA Paper No. 94-0570, AIAA, Washington, DC, 1993.
13. J. Jang and A. Hellawell: *Ironmaking Steelmaking*, 1991, vol. 18, pp. 275-83.
14. S. Ahuja: Master's Thesis, The University of Iowa, Iowa City, IA, 1992.
15. *Int. Crit. Tables Numer. Data, Phys. Chem. Technol.*, 1928, vol. 3, p. 60 and vol. 4, p. 218.
16. W.D. Bennon and F.P. Incropera: *Metall. Trans. B*, 1987, vol. 18B, pp. 611-16.
17. C. Beckermann, C. Fan, and J. Mihailovic: *Int. Video J. Eng. Res.*, 1991, vol. 1, pp. 71-82.
18. T.L. Bergman and K.S. Ball: University of Texas at Austin, Austin, TX, personal communication, 1995.
19. M.C. Flemings: *Solidification Processing*, McGraw-Hill, New York, NY, 1974.